


Article

Distribution and Enrichment Mechanisms of Selenium in Stibnite from the Xujiashan Sb Deposit, Hubei Province, China

Yuhang Liu ^{1,2}, Dazhao Wang ^{1,2,*} , Ruolong Huang ³, Guanzhi Wang ^{4,5}, Wei Wan ^{1,2,6} and Yu Kong ^{1,2}

¹ State Key Laboratory of Nuclear Resources and Environment, East China University of Technology, Nanchang 330013, China; 13700614696@163.com (Y.L.); 201760026@ecut.edu.cn (W.W.); 15925078851@163.com (Y.K.)

² National Key Laboratory of Prospecting, Mining and Remote Sense Detecting on Uranium Resources, Nanchang 330013, China

³ Forth Geological Team of Hubei Geological Bureau, Xianning 437100, China; hrl18062320512@163.com

⁴ State Key Laboratory of Geological Processes and Mineral Resources, China University of Geosciences, Beijing 100083, China; wgz_self@163.com

⁵ School of Earth Sciences, China University of Geosciences (Beijing), Beijing 100083, China

⁶ Key Laboratory of Geochemical Exploration, Institute of Geophysical and Geochemical Exploration, CAGS, Langfang 065000, China

* Correspondence: wangdazhao@ecut.edu.cn

Abstract: The Xujiashan Sb deposit located at the Mufushan fold thrust belt of the Yangtze block is one of the most important Sb deposits in this district. Stibnite in this deposit contains high and various contents of Se, but research on the distribution and enrichment of Se in stibnite remains limited. This paper conducts geochemical composition, C-H-O isotopic composition, and scanning electron microscopy morphology of the Xujiashan deposit to discuss the sources of ore-forming materials and fluid, as well as the distribution and enrichment mechanisms of selenium in stibnite. The results showed that the ores have trace element compositions comparable with the wall rocks, and Sb and Se contents are significantly higher than the average carbonate rocks. The $\delta^{13}\text{C}_{\text{PDB}}$ values of calcite and quartz range from -12.8‰ to 5.5‰ , the $\delta^{18}\text{O}_{\text{SMOW}}$ values range from 20.4‰ to 24‰ , and the $\delta\text{D}_{\text{V-SMOW}}$ values range from -57.8‰ to -86.9‰ . Trace element and isotope compositions indicate that the ore-forming materials were mainly derived from the wall rocks (sedimentary–metamorphic rocks) that S, Se, and Sb dissolved during fluid–rock interactions. The ore-forming fluids were metamorphic water produced by metamorphism, which had experienced multistage mixing with meteoric water and organic-rich fluids. Selenium substitutes for sulfur in the stibnite crystal lattice, causing rhythmically distributed Se contents in stibnite, which resulted from multistage physicochemical changes in ore-forming fluids during crystallization. The varied patterns of Se contents are the result of different cross-sections of the stibnite.

Keywords: stibnite; Se distribution and enrichment; crystal growth model; genesis of ore deposit; Xujiashan Sb deposit



Citation: Liu, Y.; Wang, D.; Huang, R.; Wang, G.; Wan, W.; Kong, Y. Distribution and Enrichment Mechanisms of Selenium in Stibnite from the Xujiashan Sb Deposit, Hubei Province, China. *Minerals* **2024**, *14*, 684. <https://doi.org/10.3390/min14070684>

Academic Editors: Francisco J. González and Jiří Sejkora

Received: 27 April 2024

Revised: 9 June 2024

Accepted: 27 June 2024

Published: 29 June 2024



Copyright: © 2024 by the authors. Licensee MDPI, Basel, Switzerland. This article is an open access article distributed under the terms and conditions of the Creative Commons Attribution (CC BY) license (<https://creativecommons.org/licenses/by/4.0/>).

1. Introduction

Antimony deposits are commonly found in the continental crusts, with many ultralarge deposits developing around the Pacific Ocean [1]. Antimony deposits in China mainly distribute in four metallogenic belts: the South China, Kunlun–Qinling, Tibet–Yunnan, and Yinshan–Tianshan belts (Figure 1a) [2,3]. Selenium (Se) has four valence states (VI, IV, 0, and $-II$) in nature, and the crustal abundance is 0.05×10^{-6} [4]. Generally, Se does not form independent ore deposits but mainly occurs as an associated element in porphyry, epithermal, orogenic, and VMS deposits [5,6]. Selenium often incorporates into the lattice of stibnite to form Sb–S–Se system; this system can further be divided into stibnite [$\text{Se}/(\text{S} + \text{Se}) < 0.20$], selenium stibnite [$0.20 \leq \text{Se}/(\text{S} + \text{Se}) < 0.50$], sulfur antimonselite [$0.50 \leq \text{Se}/(\text{S} + \text{Se}) < 0.80$], and antimonselite [$\text{Se}/(\text{S} + \text{Se}) > 0.80$] [7,8].

The Xujiashan Sb deposit is located at the southern part of the Echeng–Damushan subuplift zone within the E’Dongnan uplift belt, Hubei Province (Figure 1a). It is the largest Sb deposit in this district, is controlled by Doushantuo Formation (carbonate rocks) and fractures [9]. Many studies have been conducted on the genesis, stable isotopes, and fluid inclusions of this deposit [9–19]. For example, Sun studied the geological characteristics of the ore bodies and determined that this deposit is controlled by strata, lithology, and fractures, with evidence of sedimentary modification; Yu investigated the chemical composition, fluid inclusions, and the sulfur, oxygen, and lead isotopic compositions of stibnite, concluding that mineralization underwent hydrothermal alteration and classifying the deposit as a sedimentation–reformation antimony deposit [11,15–17]; Shen analyzed various stable isotopes and suggested that the ore-forming fluids exhibited characteristics of low to moderate temperature, low salinity, and moderate density, likely derived from deep-circulating meteoric water [9,12–14,18]. This deposit has high Se contents [10], with Se reserves reaching a medium-sized deposit [5,11]; however, the migration, distribution, and enrichment processes of Se are rarely studied.

In this study, we carried out whole-rock trace element analysis, stable isotope analysis, scanning electron microscopy–energy dispersive spectrometer (SEM-EDS) and electron probe microanalysis (EPMA) to investigate the source of ore-forming metals and reveal the distribution, occurrence, and migration mechanisms of Se in the stibnite at Xujiashan.

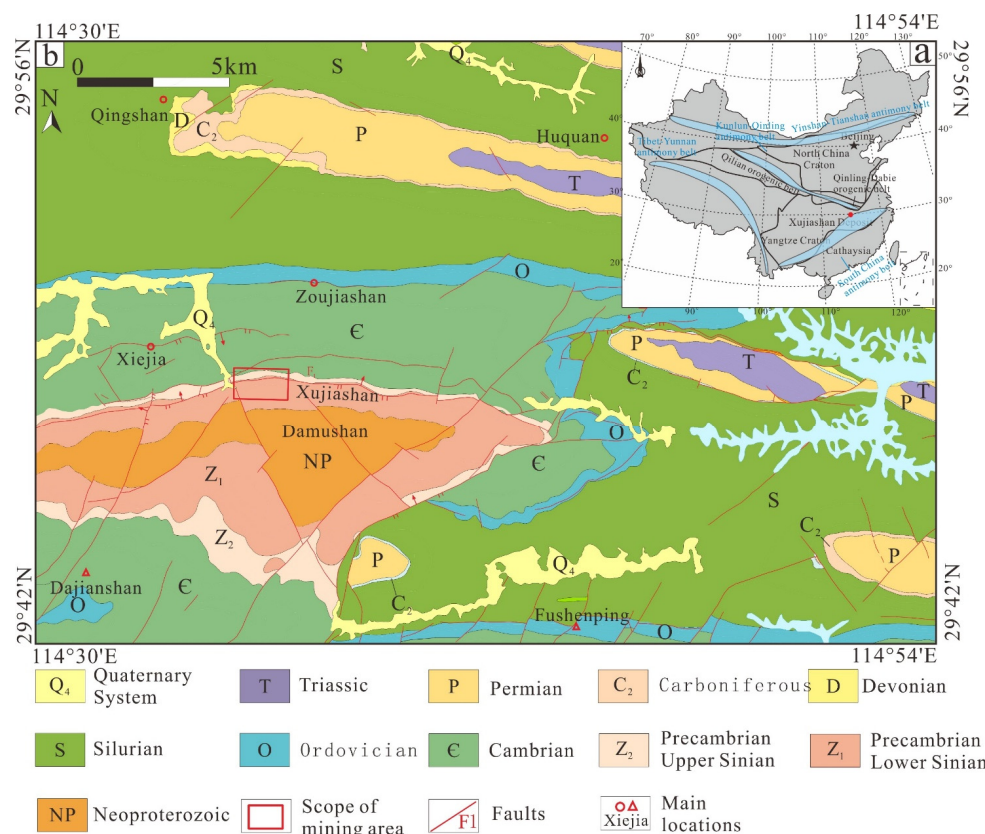


Figure 1. (a) Tectonic framework and (b) regional geological map of the Xujiashan Sb deposit (rectangle refers to Figure 2, modified after [15]).

2. Ore Deposit Geology

The Xujiashan deposit is located at the Mufushan fold thrust belt of the Yangtze block [14,16]. The lithology primarily consists of carbonate rocks, clastic rocks, and mudstone. The lithology of exposed strata includes sandstone (Neoproterozoic Liantuo Formation) and pebbled mudstone (Nantuo Formation), carbonate rocks (Upper Precambrian Doushantuo Formation) and silicalite (Laobao Formation), and carbonate rocks (Cambrian

Niutitang Formation, Figure 1b). The Doushantuo Formation is mainly composed of limestone and dolomite with small amount of shale and mudstone, and this formation can be further divided into seven lithological sections, with the Sb orebodies predominantly located in the fifth section.

This region has undergone multiple tectonic events, including the Jinning Movement and the Indosinian–Yanshanian compression and thrusting phases. The district features a complex fault structure, primarily characterized by EW-trending faults, with some NE- and near SN-trending faults. The EW-trending faults primarily control the distribution of deposits. The Xujiashan fault (F_1) is the most significant fault in the deposit, extending 18 km and intersecting the Doushantuo Formation. Igneous rocks are rare in this district [11].

Wall rock alterations in this region mainly include silicification, calcification, and baritization [18]. Silicification is widespread and can be categorized into pervasive and vein types. Calcification often overlaps with vein silicification and can be divided into pre-mineralization, syn-mineralization, and post-mineralization stages, with calcite veins present in both the pre-mineralization and syn-mineralization stages. Baritization generally coexists with silicification, calcification, and stibnite mineralization.

Orebodies at Xujiashan are clearly controlled by both faults and strata, and they can be divided into three ore belts: Sb-I, Sb-II, and Sb-III. The Sb-I and Sb-II belts are controlled by the F_1 fault, while the Sb-III belt is situated at the contact boundary between the Niutitang and Doushantuo Formations. The orebodies appear as layered, lenticular, and finely veined disseminated aggregates (Figure 2), with EW strikes, northward dips, and dip angles of 52° to 85° [19]. Individual ore bodies vary in length from 20 to 325 m, with thicknesses ranging from 0.6 to 7.84 m and dip extensions of 20 to 230 m [19]. The primary ore mineral is stibnite, accompanied by minor amounts of pyrite, sphalerite, and antimony oxides [18]. Gangue minerals include quartz, calcite, and barite, with zircon, apatite, and feldspar present as accessory minerals [19].

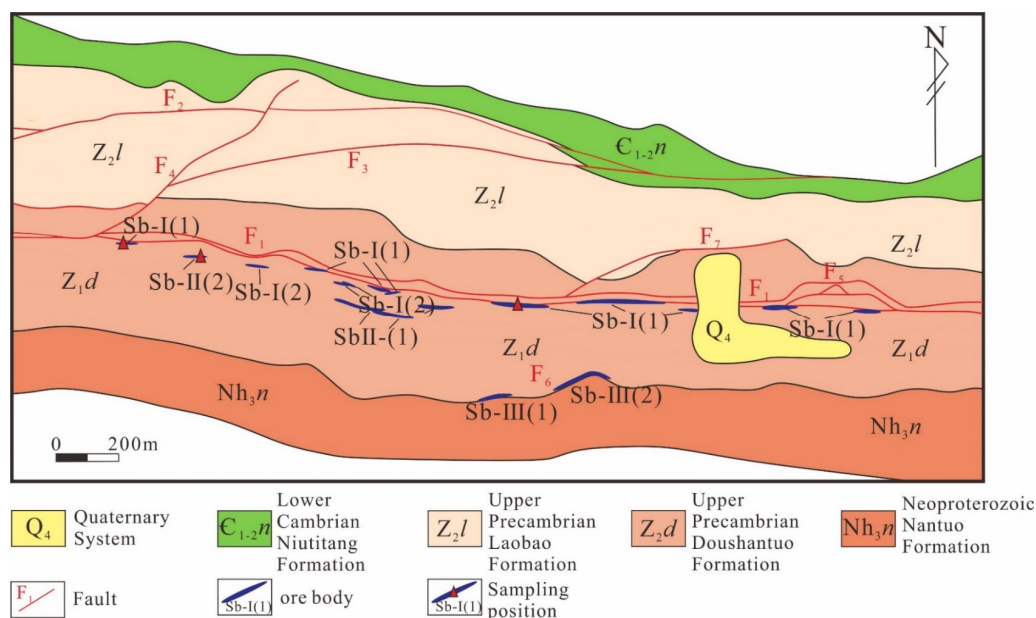


Figure 2. Geological map of the Xujiasha Sb deposit (modified after [16]). Abbreviations: Sb = Stibnite.

3. Analytical Methods

The samples in this study were primarily collected from outcrops in the Sb-I and Sb-II zones, mainly stibnite ores containing quartz and calcite.

The morphology and composition analysis for stibnite was conducted at the State Key Laboratory of Nuclear Resources and Environment, East China University of Technology (Nanchang, China). The instrument used was a ZEISS Sigma 300 field emission scanning

electron microscope equipped with an Oxford Ultim Max 100 energy dispersive spectrometer (EDS). The scanning electron microscope was operated at an acceleration voltage of 20 kV and an emission current of 10 μ A [20]. The program AZtecMineral was used to conduct automated EDS mapping over wide areas.

Electron probe microanalysis (EPMA) was performed using a JEOL JXA-8250F electron probe microanalyzer with four wavelength-dispersive spectrometers (WDS) at the State Key Laboratory of Nuclear Resources and Environment, East China University of Technology (Nanchang, China). For detailed methods, see [21–23]. The samples were coated with a thin conductive carbon film prior to the analysis. The analytical parameters are as follows: 15 kV accelerating voltage; 20 nA beam current; 5 μ m beam diameter; and counting times: 20 s (for Se, Fe, Zn, Co, Cu, S, Sb, W, Mo, and Pb), 50 s (for As), and 100 s (for Ag). Raw X-ray intensities were corrected using a ZAF correction procedure, a correction taking into account the following three effects on the characteristic X-ray intensity when performing quantitative analysis: (1) atomic number (Z) effect, (2) absorption (A) effect, and (3) fluorescence excitation (F) effect. A series of natural and synthetic SPI standards were utilized and changed based on the analyzed minerals [24]. The following standards were used: chalcopyrite (Cu, Fe, and S), synthetic gallium arsenide (As), natural galena (Pb), natural stibnite (Sb), synthetic pure silver (Ag), synthetic pure cobalt (Co), synthetic pure tungsten (W), natural sphalerite (Zn), synthetic cadmium selenide (Se), and natural molybdenite (Mo). The detection limits are 0.01 wt.% (for Se, Fe, Zn, Co, Cu, W, Mo, Pb, As, and Ag) and 0.04 wt.% (for S and Sb). Accuracy and precision are within $\pm 2\%$ relative for major elements.

Trace element analyses of whole-rock samples were completed at the ALS Global (Guangzhou, China) Co., Ltd., using an Agilent 7700x ICP-AES and an Agilent VISTA ICP-MS, with testing accuracies of 5% for rare earth elements and 5–12% for other trace elements.

Samples for C, H, and O isotope analyses were hand-selected and checked under a binocular microscope to ensure a purity of >98%. The C, H, and O isotopes were analyzed using a MAT-253 stable isotope ratio mass spectrometer at Yanduzhongshi Geological Analysis Laboratories Ltd. (Beijing, China). The techniques employed to measure H and O isotopes were according to [25,26]. The analytical precision was $\pm 0.2\%$ for $\delta^{18}\text{O}$ and $\delta^{13}\text{C}$ and $\pm 2\%$ for δD . The $\delta^{18}\text{O}$ isotopic ratios were reported in standard δ notation (‰) relative to SMOW, and the $\delta^{13}\text{C}$ isotopic ratios were reported in standard δ notation (‰) relative to PDB.

4. Results

4.1. Morphology and Structure of Ore

The ores of the Xujiashan deposit are primarily hosted within the dolomite and limestone of the Doushantuo Formation, exhibiting distinct banded structures (Figure 3a). The orebodies are stratified and lens-like, with attitudes consistent with the surrounding wall rocks. Stibnite samples are lead-gray in color (Figure 3b), and fine-grained stibnite is observed within the limestone, showing obvious calcitization (Figure 3c). Stibnite commonly coexists with quartz and calcite, and occasionally, calcite veins intersect quartz (Figure 3d). Stibnite displays a white to grayish-white reflective color and often covers and replaces quartz (Figure 3e). It also exhibits schistose textures with common deformation bands, deformation twins, and microfractures (Figure 3e,f).

Under back-scattered electron images, stibnite shows uniform chemical compositions; however, EDS analysis reveals rhythmic variations in Se content within the stibnite (see Figures 4 and 5). Selenium within stibnite contains at least three distribution patterns, including ring-like, triangular, and core–mantle patterns (Figures 4d and 5e). The width of the Se-rich belts varies.

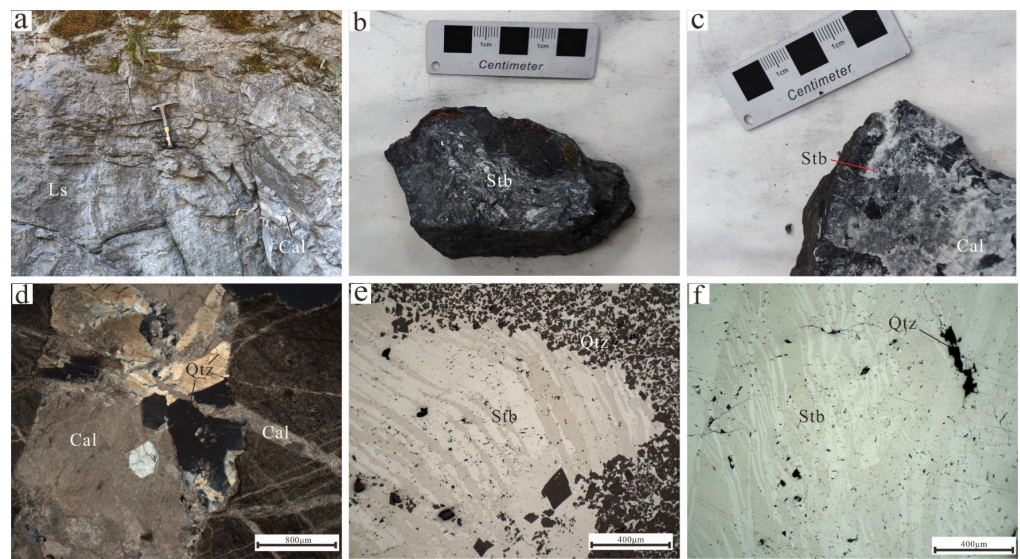


Figure 3. Photographs and photomicrographs of Xujiashan stibnite deposit: (a) The gray limestone of Doushantuo Formation; (b) Photograph of lead-gray stibnite ore, showing massive texture; (c) The limestone contains fine-grained stibnite, showing obvious calcitization; (d) Quartz is associated with calcite (e) Anisotropy of stibnite due to deformation twins in reflected light microscopy; (f). Typical en echelon deformation twins (gray) in reflected light microscopy. Abbreviations: Ls = Limestone, Cal = Calcite, Qtz = Quartz, Stb = Stibnite.

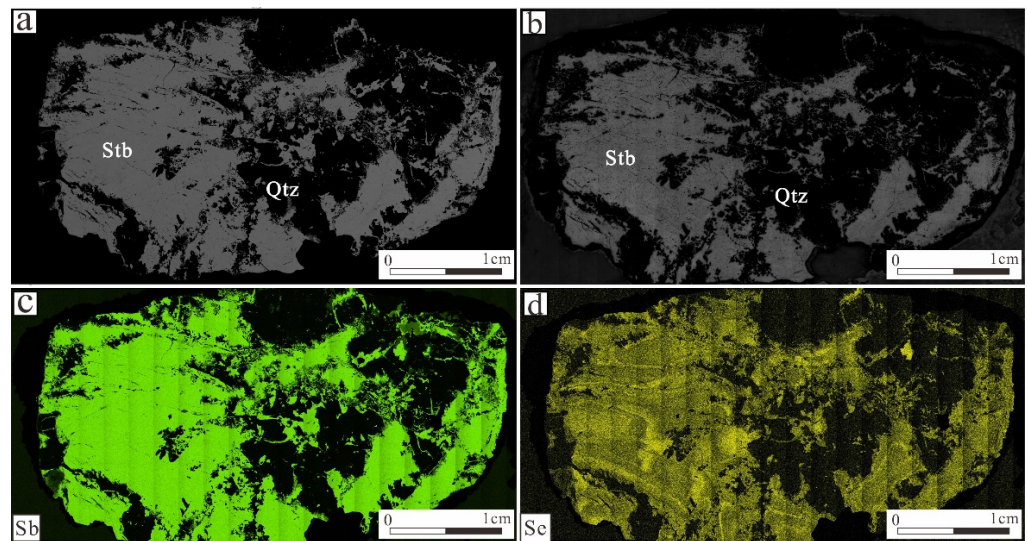


Figure 4. Microscope and scanning electron microscope images of ores from the Xujiashan deposit: (a) Back-scattered electron images; (b) Reflected light photographs of antimony ore; (c) EDS mapping of Sb contents in stibnite; (d) EDS mapping of Se contents in stibnite. Abbreviations: Qtz = Quartz, Stb = Stibnite.

4.2. EPMA Analysis

The main element compositions of stibnite in the Xujiashan deposit are 68.55% to 74.06% for Sb, 21.49% to 28.27% for S, and below detected limits to 2.44% for Se (Table 1). Based on the $\text{Se}/(\text{S} + \text{Se})$ ratio (atomic ratio), the series of stibnite–antimonelite minerals can be divided into stibnite [$\text{Se}/(\text{S} + \text{Se}) < 0.20$], selenium stibnite [$0.20 \leq \text{Se}/(\text{S} + \text{Se}) < 0.50$], sulfur antimonelite [$0.50 \leq \text{Se}/(\text{S} + \text{Se}) < 0.80$], and antimonelite [$\text{Se}/(\text{S} + \text{Se}) > 0.80$] [7,8,27–29].

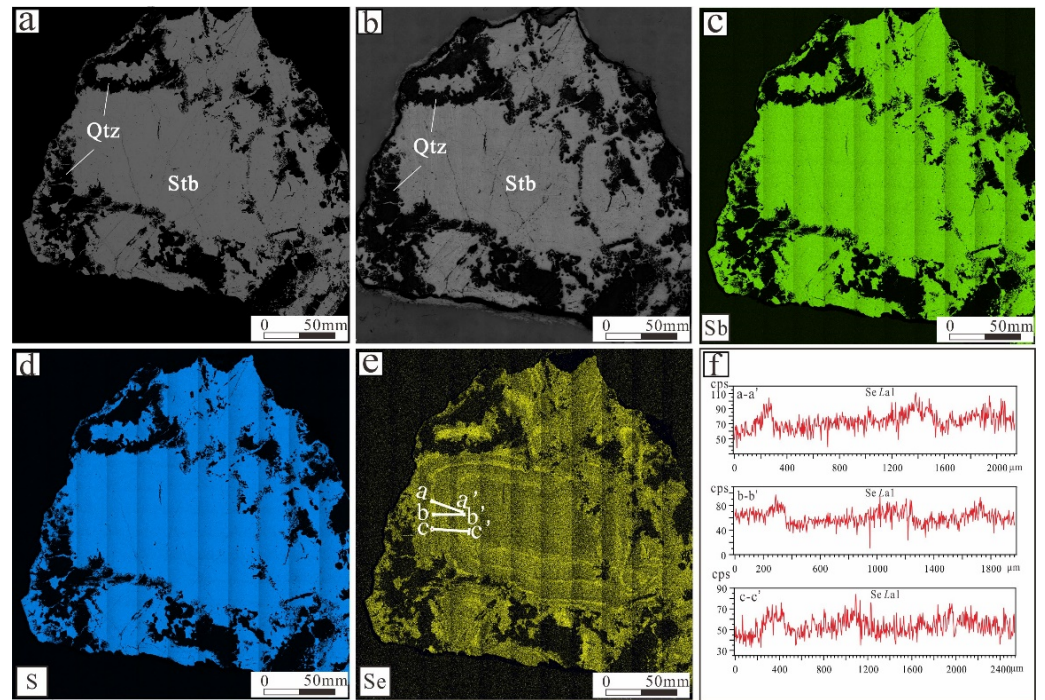


Figure 5. Microscope and scanning electron microscope images of ores from the Xujiashan deposit: (a) Back-scattered electron images of stibnite; (b) Reflected light photographs of stibnite; (c) EDS mapping of Sb contents in stibnite; (d) EDS mapping of S contents in stibnite; (e) EDS mapping of Se contents in stibnite and locations of line scanning; (f) EDS line scanning show changes in Se contents in stibnite. Abbreviations: Qtz = Quartz, Stb = Stibnite.

Based on the average chemical composition obtained by electron microprobe analysis, the chemical formula of stibnite was $Sb_{2.05}(S_{2.97}, Se_{0.03})_{3.00}$, abbreviated as $Sb_2(S, Se)_3$, belonging to selenium stibnite. Figure 6 shows that S and Se contents in stibnite vary greatly with S contents decreasing as the Se contents increase.

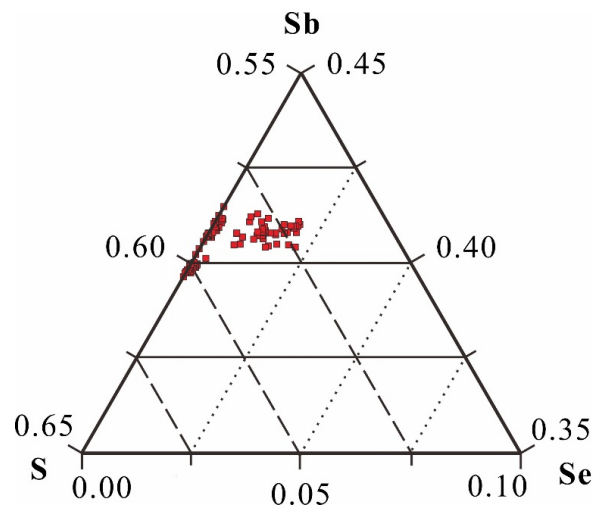


Figure 6. Composition of selenium stibnite from the Xujiashan deposit. (The red rectangles represent analysis sample).

Table 1. EPMA analyses and chemical formulae of stibnite from the Xujiashan deposit.

Samples		Zn	Cu	Sb	S	Fe	Mo	Ag	W	As	Co	Pb	Se	Molecular Formulas
		wt/%												
1004(16)	max	1.06	0.05	73.11	27.64	0.05	0.35	0.05	0.18	0.47	0.04	0.08	0.04	Sb _{2.05–2.13} S _{3.00}
	min	--	--	71.27	26.84	--	0.20	--	--	0.30	--	--	--	
	median	0.91	0.04	72.23	27.38	0.01	0.29	0.03	0.12	0.39	0.03	0.05	0.04	
1013(10)	max	0.05	0.03	71.08	28.27	0.03	0.24	0.01	0.17	0.41	0.02	0.08	0.10	Sb _{1.98–2.00} S _{3.00}
	min	--	--	70.34	27.90	--	0.20	--	--	0.20	--	--	--	
	median	0.04	0.03	70.71	28.02	0.02	0.22	0.01	0.10	0.30	0.01	0.03	0.03	
1019(10)	max	0.07	0.06	70.49	27.95	0.02	0.23	0.03	0.01	0.40	0.01	0.11	0.08	Sb _{1.98–2.03} S _{3.00}
	min	--	--	69.05	27.21	--	0.19	--	--	0.18	--	--	--	
	median	0.03	0.04	70.20	27.63	0.01	0.21	0.01	0.07	0.34	0.01	0.05	0.05	
1028(21)	max	0.945	0.07	72.63	27.18	0.07	0.40	0.06	0.13	0.60	0.03	0.11	2.26	Sb _{2.04–2.10} (S _{2.90–2.97} , Se _{0.03–0.10}) _{3.00}
	min	--	--	70.74	26.18	--	0.20	--	--	0.40	--	--	0.74	
	median	0.07	0.03	71.33	26.64	0.03	0.31	0.03	0.06	0.48	0.02	0.03	1.33	
1030(19)	max	0.99	0.08	71.61	26.66	0.05	0.38	0.05	0.10	0.62	0.03	0.11	2.44	Sb _{2.04–2.09} (S _{2.90–2.94} , Se _{0.06–0.11}) _{3.00}
	min	--	--	70.27	25.74	--	0.21	--	--	0.37	--	--	1.35	
	median	0.48	0.04	71.01	26.29	0.03	0.27	0.03	0.06	0.42	0.02	0.04	1.93	
1032(10)	max	0.07	0.06	70.97	28.03	0.01	0.26	0.03	0.12	0.34	0.02	0.15	0.18	Sb _{1.98–2.00} (S _{2.99–3.00} , Se _{0.00–0.01}) _{3.00}
	min	--	--	70.30	27.65	--	0.18	--	--	0.23	--	--	0.06	
	median	0.05	0.02	70.51	27.85	0.01	0.21	0.01	0.06	0.31	0.01	0.12	0.14	
1035(16)	max	1.06	0.08	74.06	27.90	0.06	0.36	0.09	0.14	0.60	0.04	0.07	0.31	Sb _{2.01–2.10} (S _{2.99–3.00} , Se _{0.00–0.01}) _{3.00}
	min	--	--	68.55	26.72	--	0.21	--	--	0.30	--	--	0.01	
	median	0.10	0.03	72.74	27.55	0.04	0.31	0.04	0.09	0.46	0.01	0.02	0.13	

-- represents below detection limit. The complete EPMA data are presented in Supplementary Material Table S1.

4.3. Trace Elements

The trace element contents of the ores and wall rocks in the Xujiashan deposit are comparable (Figure 7). Apart from higher concentrations of Ti, Cu, Ge, As, Se, Hf, W, and Pb, the trace element compositions of the ores and wall rocks align with those of average carbonate rocks [30]. The ores exhibit significant enrichment in As (640×10^{-6} to 730×10^{-6}), Se ($>1000 \times 10^{-6}$), Sb ($>10,000 \times 10^{-6}$), and Pb (7.00×10^{-6} to 300×10^{-6}), while being depleted in Mg, Ca, Mn, Ni, Sr, and Ce (Table 2). The elevated Sb and Se content in both the ore and wall rock suggests that the wall rocks could have contributed materials for mineralization.

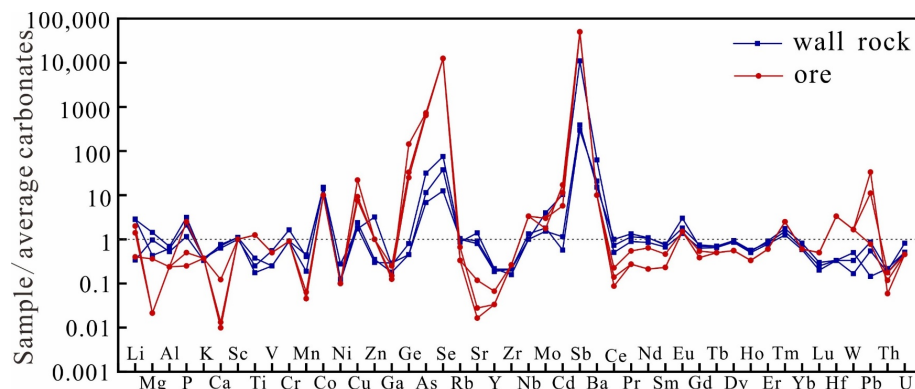


Figure 7. Trace element concentrations of wall rocks and ores from the Xujiashan deposit, ores and wall rocks normalized to the average carbonates [30].

Table 2. Comparison the trace elements of ores, wall rocks and strata(rocks) from the Xujiashan deposit ($\times 10^{-6}$).

Samples	Detection Limit	XJS-2001	XJS-2002	XJS-2003	XJS-2004	XJS-2005	XJS-2006	Turekian and Wedepohl [30]		
		Wall Rock	Wall Rock	Wall Rock	Ore	Ore	Ore	Shales	Carbonates	Clay
Li	0.20	14.30	14.10	1.70	10.0	7.00	2.00	66.0	5.00	57
Be	0.05	0.14	0.30	0.20	0.50	0.50	0.50	3.00	--	2.60
Mg	100	20,200	67,200	45,500	1000	1000	17,000	15,000	47,000	21,000
Al	100	2600	2900	2200	1000	1000	1000	80,000	4200	84,000
P	10.0	840	1260	460	100	200	1000	700	400	1500
K	100	1000	1000	900	1000	1000	1000	26,600	2700	25,000
Ca	100	215,000	191,000	230,000	3000	4000	37,000	22,100	302,300	29,000
Sc	0.10	1.10	1.00	1.10	1.00	1.00	1.00	13.0	1.00	19.0
Ti	50.0	150	100	70.0	500	500	500	4600	400	4600
V	5.00	5.00	11.0	5.00	10.0	10.0	10.0	130	20.0	120
Cr	1.00	10.0	18.0	10.0	10.0	10.0	10.0	90.0	11.0	90.0
Mn	5.00	207	447	488	50.0	50.0	70.0	850	1100	6700
Co	0.10	1.50	1.50	1.40	--	--	--	19.0	0.10	74.0
Ni	0.20	2.20	5.50	2.50	2.00	2.00	2.00	68.0	20.0	225
Cu	0.20	7.30	6.90	9.60	88.0	30.0	37.0	45.0	4.00	250
Zn	2.00	6.00	64.0	7.00	20.0	20.0	20.0	95.0	20.0	165
Ga	0.05	1.16	1.04	0.72	0.50	1.00	0.60	19.0	4.00	20.0
Ge	0.05	0.09	0.16	0.09	28.7	6.60	5.00	1.60	0.20	2.00
As	0.20	6.80	31.5	11.4	730	720	640	13.0	1.00	13.0
Se	1.00	1.00	6.00	3.00	>1000	>1000	>1000	0.60	0.08	0.17
Rb	0.20	3.10	3.00	2.60	1.00	2.00	1.00	140	3.00	110
Sr	0.20	561	486	854	10.0	17.0	72.0	300	610	180
Y	0.10	6.30	5.60	6.50	1.00	1.00	2.00	26.0	30.0	90.0
Zr	2.00	4.00	4.00	3.00	5.00	5.00	5.00	160	19.0	150
Nb	0.10	0.40	0.30	0.30	1.00	1.00	1.00	11.0	0.30	14.0
Mo	0.05	0.72	1.59	0.61	1.20	0.70	1.20	2.60	0.40	27.0

Table 2. Cont.

Samples	Detection Limit	XJS-2001	XJS-2002	XJS-2003	XJS-2004	XJS-2005	XJS-2006	Turekian and Wedepohl [30]		
		Wall Rock	Wall Rock	Wall Rock	Ore	Ore	Ore	Shales	Carbonates	Clay
Ag	0.01	0.06	0.06	0.04	1.20	1.10	0.50	0.07	--	0.11
Cd	0.02	0.02	0.36	0.04	0.40	0.60	0.20	0.30	0.035	0.42
In	0.005	0.005	0.005	0.011	0.08	0.05	--	0.10	--	0.08
Sn	0.2	--	--	--	2.00	2.00	2.00	6.00	--	1.50
Sb	0.05	59.3	2200	78	>10,000	>10,000	>10,000	1.50	0.2	1.00
Cs	0.05	0.63	0.66	0.32	--	--	--	5.00	--	6.00
Ba	0.50	209	626	151.5	100.00	100.00	100.00	580	10.0	2300
La	0.10	4.10	5.50	7.50	34.00	40.00	34.00	92.0	--	115
Ce	0.10	5.8	8.40	11.5	1.00	1.60	2.60	59.0	11.5	345
Pr	0.02	0.98	1.26	1.46	0.30	0.30	0.60	5.60	1.10	33.0
Nd	0.10	4.00	5.00	5.10	1.00	1.00	3.00	24.0	4.70	140
Sm	0.03	0.87	1.01	0.96	0.30	0.30	0.60	6.40	1.30	38.0
Eu	0.02	0.27	0.36	0.60	0.30	0.30	0.30	1.00	0.20	6.00
Gd	0.05	0.82	0.97	0.89	0.50	0.50	0.70	6.40	1.30	38.0
Tb	0.01	0.13	0.14	0.14	0.10	0.10	0.10	1.00	0.20	6.00
Dy	0.05	0.78	0.77	0.84	0.50	0.50	0.50	4.60	0.90	27.0
Ho	0.01	0.16	0.15	0.17	0.10	0.10	0.10	1.20	0.30	7.50
Er	0.03	0.46	0.39	0.42	0.30	0.30	0.30	2.50	0.50	15.0
Tm	0.01	0.07	0.05	0.06	0.10	0.10	0.10	0.20	0.04	1.20
Yb	0.03	0.41	0.29	0.32	0.30	0.30	0.30	2.60	0.50	15.0
Lu	0.01	0.06	0.04	0.05	0.10	0.10	0.10	0.70	0.20	4.50
Hf	0.10	0.10	0.10	0.10	1.00	1.00	1.00	2.80	0.30	4.10
Ta	0.05	--	--	--	--	--	--	0.80	--	--
W	0.1	0.30	0.20	0.10	1.00	1.00	1.00	1.80	0.60	--
Tl	0.02	0.04	0.11	0.02	0.50	0.40	1.10	1.40	--	0.80
Pb	0.50	1.30	7.80	4.90	300	7.00	100	20.0	9.00	80.0
Th	0.05	0.37	0.33	0.30	0.10	0.20	0.30	12.0	1.70	7.00
U	0.05	1.12	1.79	1.11	--	--	1.00	3.70	2.20	1.30
Hf/Sm	--	0.11	0.10	0.10	3.33	3.33	1.67	--	--	--
Nb/La	--	0.10	0.05	0.04	0.03	0.03	0.03	--	--	--
Th/La	--	0.09	0.06	0.04	--	0.01	0.01	--	--	--
ΣREE	--	18.8	24.5	30.1	39.9	46.8	44.1	--	--	--
LREE	--	16.0	21.5	27.1	36.9	43.5	41.1	--	--	--
HREE	--	2.78	2.93	2.93	2.99	3.32	3.03	--	--	--
LREE/HREE	--	5.76	7.35	9.26	12.3	13.1	13.6	--	--	--
LaN/YbN	--	9.80	9.39	14.9	18.9	17.7	21.6	--	--	--
δEu	--	0.98	1.11	1.98	2.37	2.37	1.42	--	--	--
δCe	--	0.71	0.78	0.85	0.08	0.11	0.14	--	--	--

-- indicates that it did not reach the detection limit.

Cobalt (Co) is an indicator of oxygen levels in marine environments, typically lower in eutrophic waters and higher in oligotrophic waters [31]. In this study, the Co content in the wall rocks ranges from 1.40×10^{-6} to 1.50×10^{-6} , indicating a nutrient-poor environment. Molybdenum (Mo) content, ranging from 0.7×10^{-6} to 1.59×10^{-6} , suggests a weakly sulfidic environment [4]. Uranium (U) content in sedimentary rocks is typically low under oxidizing conditions, with concentrations ranging from 1×10^{-6} to 10×10^{-6} . The U content of the wall rocks in this study, ranging from 1.11×10^{-6} to 1.79×10^{-6} , indicates an oxidizing sedimentary environment [4].

The total rare earth element (REE) content of the ores ranges from 39.9×10^{-6} to 46.8×10^{-6} , with light rare earth element (LREE) contents between 36.9×10^{-6} and 43.5×10^{-6} and heavy rare earth element (HREE) content between 2.99×10^{-6} and 3.32×10^{-6} . The LREEs/HREEs ratios range from 12.34 to 13.56 and the (La/Yb) ratios from 17.71 to 21.58 (Table 2). The δEu values range from 1.42 to 2.37 and δCe values from 0.08 to 0.14 in the stibnite.

4.4. C-H-O Isotope Composition

The carbon and oxygen isotopic compositions of calcite and quartz from the Xujiashan deposit are listed in Table 3 and shown in Figure 8. The $\delta^{13}\text{C}_{\text{PDB}}$ values of calcite range from -0.8‰ to 5.5‰ , and the $\delta^{18}\text{O}_{\text{SMOW}}$ values range from 20.4‰ to 20.7‰ . The $\delta^{13}\text{C}_{\text{PDB}}$ values of quartz range from -12.8‰ to -8.1‰ , and the $\delta^{18}\text{O}_{\text{SMOW}}$ values range from 22.6‰ to 24‰ .

The hydrogen and oxygen isotope compositions of calcite and quartz are listed in Table 3. The $\delta\text{D}_{\text{V-SMOW}}$ values of calcite range from -57.8‰ to -86.9‰ , and the $\delta\text{D}_{\text{V-SMOW}}$ values of quartz range from -67.4‰ to -67.9‰ . According to the fluid inclusion homogenization temperatures obtained by Yu and Cao [11], the calculated $\delta^{18}\text{O}_{\text{H}_2\text{O}}$ values are 8.78‰ to 10.18‰ . The $\delta^{18}\text{O}_{\text{H}_2\text{O}}-\delta\text{D}$ composition of quartz and calcite are distributed within the range of metamorphic water (Figure 9).

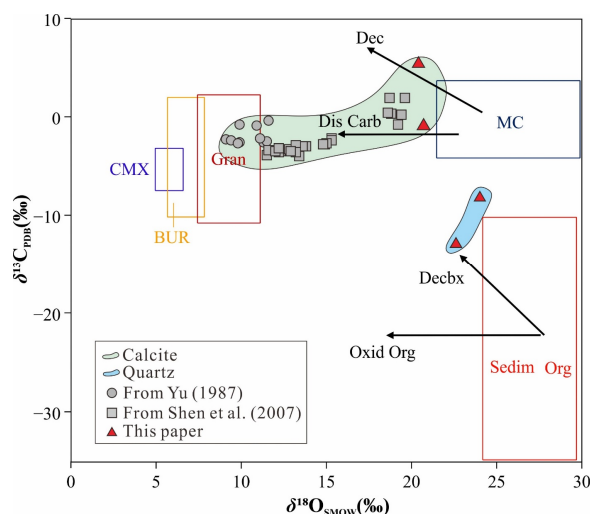


Figure 8. Plots of $\delta^{13}\text{C}$ versus $\delta^{18}\text{O}$ of calcites and quartz from the Xujiashan deposit. For reference, the fields for typical marine carbonates (MC), sedimentary organic matter (Sedim Org), igneous carbonatite and mantle xenoliths (CMX), basic and ultrabasic rocks (BUR), and granite (Gran) are outlined. The arrows show typical isotopic trends resulting from carbonate dissolution (Dis Carb), decarbonation (Dec), decarboxylation of organic matter (Decbx), oxidation of organic matter (Oxid Org), and mixing trend (MT) (modified after [32,33], part of $\delta^{13}\text{C}_{\text{PDB}}$ and $\delta^{18}\text{O}_{\text{SMOW}}$ value after [12,15]).

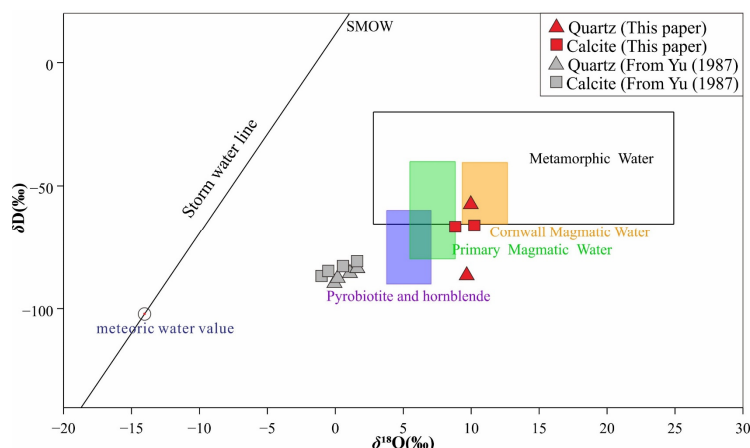


Figure 9. Plot of δD versus $\delta^{18}\text{O}_{\text{H}_2\text{O}}$ of calcites and quartz for the Xujiashan deposit (range of magmatic water, igneous hornblende, and biotite cited from [34]; Range of granite magma water cited from [35]; The extent of metamorphic water combines data from [34] and [36] (part of δD and $\delta^{18}\text{O}_{\text{SMOW}}$ value after [14], meteoric water value after [37]).

Table 3. Oxygen, carbon, and hydrogen isotopic compositions of quartz and calcite from the Xujiashan deposit.

Samples	Lithology	δD_{V-SMOW}	$\delta^{18}O_{V-SMOW}$	$\delta^{18}O_{V-PDB}$	$\delta^{13}C_{V-PDB}$	Temperature (°C)	$\delta^{18}O_{H_2O}$ (‰)
		(‰)	(‰)	(‰)	(‰)		
21XJS-3001	Quartz	−67.9	22.6	−8.02	−12.8	170	8.78
21XJS-3002	Quartz	−67.4	24.0	−6.66	−8.10	170	10.2
21XJS-3001-Ca	Calcite	−57.8	20.7	−9.90	−0.80	170	9.42
21XJS-3003-Ca	Calcite	−86.9	20.4	−10.2	5.50	170	9.12

$\delta^{18}O_{H_2O}$ was calculated using the following equilibrium temperature formula: $1000\ln_{Quartz-water} = 3.38 \times 10^6 / (T + 273.15)^2 - 3.40$ [38]. $1000\ln_{Calcites-water} = 2.78 \times 10^6 / (T + 273.15)^2 - 3.39$ [39].

5. Discussion

5.1. Sources of Ore-forming Fluid

Many models have been established for the genesis of Xujiashan deposits, including syn-sedimentary mineralization [11,15–18], infill of hydrothermal fluids in interlayer fracture zones [40], and precipitation of low- to medium-temperature hydrothermal fluids [9]. Yu and Cao concluded that the Xujiashan deposit underwent a sedimentary-mineralization stage and a hydrothermal fluid alteration stage, where the latter one precipitated stibnite, quartz, calcite, barite, and pyrite. The wall rocks exhibit antimony (Sb) contents exceeding 10 ppm (Table 4), which is 55–235 times higher than the average crustal value of 0.2 ppm. Moreover, the trace element compositions of the ores and wall rocks are similar (Figure 7), indicating that the metals for mineralization originated from the wall rocks, with the deposition of Sb in the ore-hosting strata serving as the initial enrichment stage [11]. Marine sediments and carbonate-bearing rocks are enriched in Te and Se [41,42], and organic matter is an important host for Se [43], accounting for the high Se contents in the organic matter-rich black shales of the Cambrian Niutitang Formation [44–46]. Therefore, the Niutitang Formation is a potential source for Se mineralization at Xujiashan.

Table 4. Antimony contents of strata in the Damushan district [19].

Position	Antimony Content	Crustal Antimony Abundance Value
Lengjiayi Formation	11 ppm	0.2 ppm
Nantuo Formation	28 ppm	
Liantuo Formation	23 ppm	
Doushantuo Formation	47 ppm	
Laobao Formation	39 ppm	

Yu [11,15] studied the sulfur isotopic compositions of stibnite ranging from +12.1 to +14.4, coincident with the sedimentary sulfur, indicating the origin of wall rocks or the earlier sedimentary deposits. The author also tested the oxygen, carbon, and hydrogen isotopic compositions of quartz and calcite; the $\delta^{13}C_{PDB}$ values of calcite range from −0.3‰ to −2.6‰, and the $\delta^{18}O_{SMOW}$ values range from 9.1‰ to 11.6‰. These isotopic compositions are consistent with those of marine carbonates and align with pre-mineralization calcite measurements by Shen [12], indicating a common source. The combined $\delta^{13}C_{PDB}$ and $\delta^{18}O_{SMOW}$ isotopic compositions of calcite suggest an evolutionary trend indicating a mixture of carbon sources. Quartz exhibits $\delta^{13}C_{PDB}$ values between −12.8‰ and −8.1‰, and $\delta^{18}O_{SMOW}$ values between 22.6‰ and 24‰ (Figure 8), differing from those of calcite. This discrepancy suggests distinct carbon isotope sources: carbon isotopes in calcite are primarily derived from $CaCO_3$, reflecting the source of ore-forming materials, while those in quartz are derived from fluid inclusions, indicating the C isotope composition of ore-forming fluids. Therefore, it is inferred that the ore-forming materials originated from the wall rocks. The hydrothermal fluids dissolved the wall rocks (carbonates) and underwent water–rock interactions, with some carbon in the fluids possibly derived from the decarboxylation of organic matter [47].

The $\delta^{18}\text{O}_{\text{H}_2\text{O}}$ values of calcite range from -1.06‰ to 1.57‰ [11], and the $\delta^{18}\text{O}_{\text{H}_2\text{O}}$ values of the ore-forming fluids exhibit regular variations during mineralization, indicating continuous oxygen isotope exchange between the hydrothermal fluids and the wall rocks. Kinetic fractionation causes the $\delta\text{D}-\delta^{18}\text{O}_{\text{H}_2\text{O}}$ values to skew towards higher $\delta^{18}\text{O}_{\text{H}_2\text{O}}$ values, deviating from the meteoric water line (Figure 9). Combining the δD and $\delta^{18}\text{O}_{\text{H}_2\text{O}}$ isotopic compositions with the regional meteoric water line shows a continuous evolutionary trend, suggesting that the fluid originated from a mixture of metamorphic water and meteoric water. Differences in the extent of meteoric water influence at various mineralization stages result in different positions on the diagram, but the overall evolutionary trend remains consistent. In addition, the fluid inclusions are mainly liquid inclusions with homogenization temperature ranging from 158 °C to 189 °C , significantly lower compared with the magmatic fluids but coincident with the meteoric and metamorphic fluids [11]. Thus, the ore-forming fluids are primarily deep-circulating meteoric water mixed with organic-rich fluids.

The C-H-O isotope compositions and mineral trace element compositions presented in this study indicate that the ore-forming materials were derived from sedimentary–metamorphic rocks, and the ore-forming fluids were metamorphic water produced by metamorphism. The ore-forming fluids experienced multistage mixing of meteoric water and organic-rich fluids.

5.2. Genesis and Growth Modeling of Selenium Stibnite

Stibnite (Sb_2S_3) and antimonelite (Sb_2Se_3), with the general formula $\text{A}_2\text{VB}_3\text{VI}$ (where $\text{A} = \text{Sb}$ and $\text{B} = \text{S, Se}$), are layer-structured semiconductors with orthorhombic crystal structure. In these compounds, each Sb atom is bonded to three S or Se atoms, and each S or Se atom is bonded to three Sb atoms, with the layers held together by weak secondary bonds (Figure 10) [48,49]. The chemical bonds within the ribbons are strong, whereas the bonds between the ribbons are much weaker due to the concentration of electron density within the ribbons.

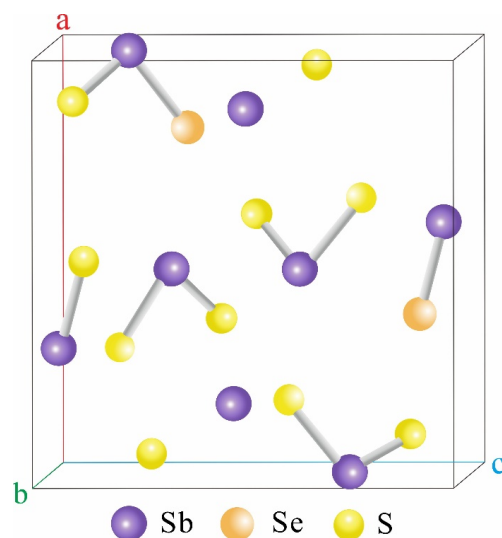


Figure 10. Crystal structure of $\text{A}_2\text{VB}_3\text{VI}$ ($\text{A} = \text{Sb}$ and $\text{B} = \text{S, Se}$).

The valence electron configurations of Sb, S, and Se are $5s^25p^3$, $3s^23p^4$, and $4s^24p^4$, respectively. The Se atom is larger than the S atom, and the inner atoms (closer to the center of the ribbons) have smaller volumes than the outer atoms (closer to the edges of the ribbons) [50]. Selenium substitutes for sulfur in the stibnite crystal lattice, causing lattice expansion. However, this expansion is minor at low Se concentrations, similar to the mechanism of arsenic substitution for sulfur in pyrite [51].

Rhythmic bands and chemical zoning in minerals indicate physicochemical changes in ore-forming fluids during crystallization, including pressure, temperature, and chemical

compositions, which are also controlled by kinetic factors and hydrothermal alteration after precipitation. Therefore, banded minerals could reveal crystallization when processed or after subsequent alteration events. For example, zircon in the Namcha Barwa Formation comprises a magmatic core and a metamorphic rim, reflecting early magmatic and subsequent metamorphic events [52–55]. Ring-banding pyroxene from the Yaojiazhuang pluton reveals multistage crystallization during magmatic mixing [56–58]. Variations in element compositions in pyrite at the Zijinshan Cu-Au deposit indicate changes in temperature and the geological environment during the precipitation of ore-forming fluids [59,60].

Stibnite from Xujiashan has Sb contents of 68.55% to 74.06% and S contents of 25.74% to 28.27% and Se contents up to 2.44% with an average value of 0.68%. The Se contents in stibnite are approximately five orders of magnitude higher than the crustal value and much higher than those in the Xikuangshan Sb deposit (9.2×10^{-6} [61]). Owing to the similar geochemical characteristics of Se and S, Se can replace S easily in sulfides and is less likely to form selenides [62,63]. EDS analyses reveal that Se is distributed rhythmically in stibnite grains, reflecting physicochemical changes during crystallization (Figures 4 and 5). Based on the distributed patterns of Se in stibnite and the origin of metals, the formation model for selenium stibnite has been established.

Hydrothermal fluids, derived from heated meteoric and metamorphic water dissolve S, Se, and Sb from wall rocks, forming ore-forming fluids. Initially, $f(\text{O}_2)$ and $f(\text{Se}_2)$ are relatively low, while $f(\text{S}_2)$ is high, favoring the precipitation of stibnite (Figure 11a). Due to the consumption of S during stibnite crystallization or mixing with Se-rich fluids, selenium stibnite precipitates and covers the early formed stibnite (Figure 11b). As the Se content decreases, stibnite precipitates again. These processes could occur multiple times and result in the rhythmically banded textures in stibnite (Figure 11c).

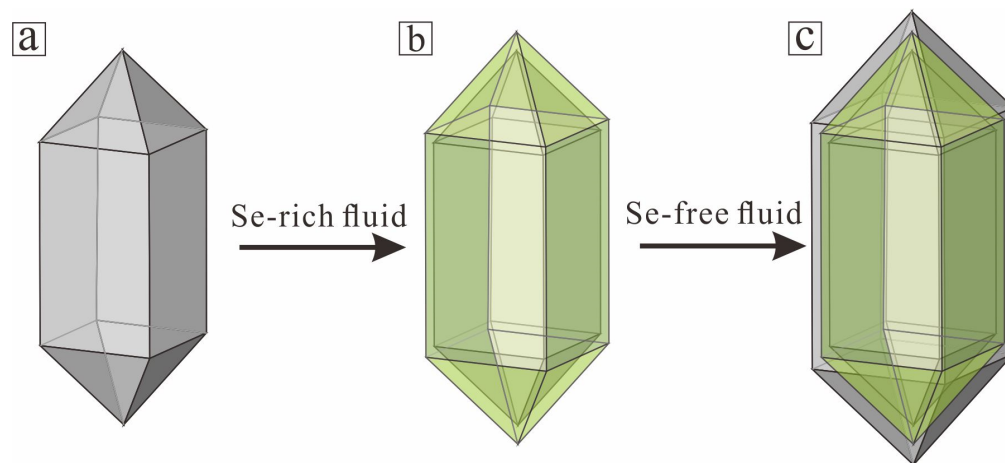


Figure 11. Crystallization processes of Se-bearing bands in stibnite: (a) precipitation of stibnite; (b) selenium stibnite precipitates and covers the early formed stibnite; (c) stibnite precipitates again.

The Se-bearing bands in the stibnite have various patterns (Figures 4 and 5), which may have resulted from different cross-sections of the stibnite. The different cross-sections of the stibnite will form different shapes of Se-bearing ring bands. If the cross-section is the crystal's transverse section (Figure 12, a-a'), a ring-shaped band will appear. If the cross-section is the crystal's surface (Figure 12, b-b'), a core-mantle ring band will appear. If the cross-section is an oblique cut crystal (Figure 12, c-c'), a rhombic or triangular ring band will appear.

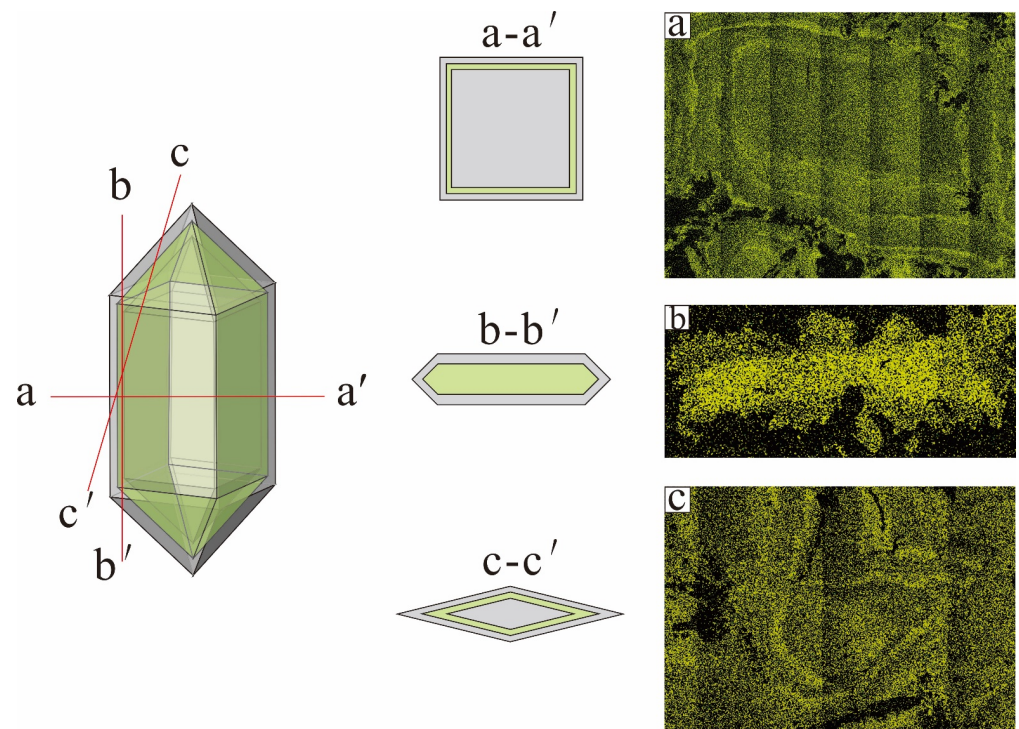


Figure 12. Various Se-bearing bands shapes of different cross-sections of stibnite: (a) The cross-section of the stibnite crystal; (b) The longitudinal section of the stibnite crystal; (c) The oblique section of the stibnite crystal.

6. Conclusions

(1) The chemical formula of stibnite in Xujiashan stibnite deposit is $Sb_{2.05}(S_{2.97}, Se_{0.03})_{3.00}$, abbreviated as $Sb_2(S, Se)_3$, belonging to selenium stibnite.

(2) The ore-forming materials were mainly derived from the wall rocks (sedimentary–metamorphic rocks). Hydrothermal fluids derived from heated meteoric and metamorphic water, which dissolved S, Se, and Sb from wall rocks, and formed ore-forming fluids. Ore-forming fluids experienced multistage mixing of meteoric water and organic-rich fluids.

(3) Selenium substitutes for sulfur in the stibnite crystal lattice, causing rhythmically distributed Se contents in stibnite, which resulted from multistage physicochemical changes in ore-forming fluids during crystallization.

Supplementary Materials: The following supporting information can be downloaded at: <https://www.mdpi.com/article/10.3390/min14070684/s1>, Table S1: EPMA analyses and chemical formulae of stibnite from the Xujiashan deposit.

Author Contributions: Conceptualization and methodology, D.W. and Y.L.; Investigation, D.W., G.W. and R.H.; Experimental analysis, Y.L., W.W. and Y.K.; Writing—original draft preparation, Y.L. and D.W.; Writing—review and editing, D.W.; Plotting, Y.L. and D.W. All authors have read and agreed to the published version of the manuscript.

Funding: This research was funded by China National Natural Science Foundation, grant numbers 92062219, the National Key R&D Program of China, grant number 2023YFC2906801, and the National Nonprofit Institute Research Grant of IGGE, grant number AS2022P03.

Data Availability Statement: Data available on request due to restrictions eg privacy or ethical: The data presented in this study are available on request from the corresponding author due to (specify the reason for the restriction).

Conflicts of Interest: The authors declare no conflicts of interest.

References

1. Yi, J.B. Basic characteristics of global antimony ore deposits and the background of mega antimony deposits. *Geotecton. Metallog.* **1994**, *18*, 199–208. (In Chinese with English Abstract)
2. Zhang, G.L.; Yao, J.Y.; Gu, X.P. Time and spatial distribution regularities and deposit types of antimony in China. *Miner. Resour. Geol.* **1998**, *12*, 19–25. (In Chinese with English Abstract)
3. Xiao, Q.M.; Zeng, D.R.; Jin, F.Q.; Yang, M.Y.; Yang, Z.F. Time-Space Distribution Feature and Exploration Guide of China's Sb-Deposits. *Geol. Explor.* **1992**, *12*, 9–14. (In Chinese with English Abstract)
4. Zhang, G.; Jiang, X.; Fan, H.F.; Wen, H.J. Selenium Enrichment in the Ediacaran Doushantuo Formation from Yichang Region, South China and Its Geology Implications. *Acta Miner. Sin.* **2017**, *37*, 258–268. (In Chinese with English Abstract)
5. Chen, B.H.; Ding, J.H.; Ye, H.S.; Yin, J.N.; Liu, J.N. Metallogenic regularity of selenium ore in China. *Miner. Deposits.* **2020**, *39*, 1063–1077. (In Chinese with English Abstract)
6. Li, J.X.; Liu, J.J. Advances in selenium resource study. *Resour. Ind.* **2014**, *16*, 90–97. (In Chinese with English Abstract)
7. Heropoulos, C.; Seeley, J.L.; Radtke, A.S. Spectrographic Determination of Selenium in Stibnite. *Appl. Spectrosc.* **1984**, *38*, 451–454. [[CrossRef](#)]
8. Liu, J.J.; Li, Z.M.; Liu, J.M.; Wang, J.P.; Feng, C.X.; Lu, W.Q. Mineralogy of the Stibnite-Antimonelite Series in the Nature. *J. Jilin Univ. (Earth Sci. Ed.)* **2005**, *35*, 545–553. (In Chinese with English Abstract)
9. Shen, N.P.; Peng, J.T.; Yuan, S.D.; Zhang, D.L.; Hu, R.Z.; Wang, G.Q. Characteristics of fluid inclusions in Xujiashan antimony deposit of Hubei Province and its implications. *Miner. Dep.* **2008**, *27*, 570–578. (In Chinese with English Abstract)
10. Zhang, D.; Wang, S.J. Mineralogical Characteristics and Geological Significance of Se, Te-Rich Stibnite in Sb Ore Belt, Southern Anhui Province. *Earth Sci. J. Chin. Univ. Geosci.* **1994**, *19*, 169–173. (In Chinese with English Abstract)
11. Yu, H.L.; Cao, W. The geological characteristics and stable isotope composition of the xujiashan antimony deposit in Hubei province and its mechanism of ore formation. *Geol. Rev.* **1986**, *32*, 264–275+322. (In Chinese with English Abstract)
12. Shen, N.P.; Peng, J.T.; Yuan, S.D.; Zhang, D.L.; Fu, Y.Z.; Hu, R.Z. Carbon, oxygen and strontium isotope geochemistry of calcites from Xujiashan antimony deposit, Hubei Province. *Geochimica* **2007**, *36*, 479–485. (In Chinese with English Abstract)
13. Shen, N.P.; Peng, J.T.; Yuan, S.D.; Zhang, D.L.; Hu, R.Z.; Wang, G.Q. Sm-Nd isotope system of calcite from Xujiashan antimony deposit, Hubei, China-Possibility of its Caledonian mineralization. In Proceedings of the 12th Annual Conference of Mineralogy, Petrology and Geochemistry Society of China, Guiyang, China, 2009. (In Chinese with English Abstract).
14. Shen, N.P.; Peng, J.T.; Yuan, S.D.; Zhang, D.L.; Hu, R.Z. Lead isotope compositions and its significance for ore-forming material of the xujiashan antimony deposit, Hubei province. *Acta Mineral. Sin.* **2008**, *02*, 169–176. (In Chinese with English Abstract)
15. Yu, H.L. The material source of and the properties of ore-forming solutions responsible for strata bound Sb deposits in carbonate rocks at xujiashan, Hubei province. *Geochimica* **1987**, *2*, 167–175. (In Chinese with English Abstract)
16. Sun, H.Z.; Lei, L. Geological characteristics of the xujiashan stratified antimony deposit in Hubei province. *Miner. Depos.* **1988**, *7*, 49–54. (In Chinese with English Abstract)
17. Yu, H.L. Typomorphic characteristics of stibnite from Xujiashan. Hubei province with a discussion on its genesis. *Acta Petrol. Miner.* **1988**, *7*, 361–367. (In Chinese with English Abstract)
18. Shen, N.P.; Peng, J.T.; Hu, R.Z.; Liu, S.; Coulson, I.M. Strontium and Lead Isotopic Study of the Carbonate-hosted Xujiashan Antimony Deposit from Hubei Province, South China: Implications for its Origin. *Resour. Geol.* **2011**, *61*, 52–62. [[CrossRef](#)]
19. The fourth geological Brigade, Hubei Geological Bureau. (Tongshan County, Hubei Province, China). Personal communication, 2023.
20. Shen, Q.W.; Wang, D.Z.; Leng, C.B.; Yu, H.J.; Zhang, C.Y.; Su, X.Y.; Mao, J.W.; Liang, F. Discovery of Telluride and Selenide in the Giant Pulang Porphyry Cu-Au Deposit, Yunnan Province. *Rock Min. Anal.* **2023**, *42*, 643–646. (In Chinese with English Abstract)
21. Guo, G.L.; Xu, X.Z.; Li, J.Y. The character and genesis of anorthite as inclusions in spinel of mantle peridotites from the Purang ophiolite (Southwestern Tibetan Plateau). *Acta. Petrol. Sin.* **2011**, *27*, 3197–3206. (In Chinese with English Abstract)
22. Liu, C.Z.; Wu, F.Y.; Wilde, S.A.; Yu, L.J.; Li, J.L. Anorthitic plagioclase and pargasitic amphibole in mantle peridotites from the Yungbwa ophiolite (southwestern Tibetan Plateau) formed by hydrous melt metasomatism. *Lithos* **2010**, *114*, 413–422. [[CrossRef](#)]
23. Xu, X.Z.; Yang, J.S.; Guo, G.L.; Li, J.Y. Lithological research on the Purang mantle peridotite in western Yarlung-Zangbo suture zone in Tibet. *Acta. Petrol. Sin.* **2011**, *27*, 3179–3196. (In Chinese with English Abstract)
24. Hu, H.; Wang, R.C.; Xie, L.; Zhang, W.L.; Tian, E.R.; Xu, Y.T.; Fan, H.R. High Precision Analysis of Chemical Composition of SPI Monazite Standard on Large Spectrometer of 140 mm Rowland Circle. *Geol. J. Chin. Uni.* **2021**, *27*, 317–326. (In Chinese with English Abstract)
25. Coleman, M.L.; Sheppard, T.J.; Durham, J.J.; Rouse, J.E.; Moore, G.R. Reduction of water with zinc for hydrogen isotope analysis. *Anal. Chem.* **1982**, *54*, 993–995. [[CrossRef](#)]
26. Clayton, R.N.; Mayeda, T.K. The use of bromine pentafluoride in the extraction of oxygen from oxides and silicates for isotopic analysis. *Geochim. Cosmochim. Acta* **1963**, *27*, 43–52. [[CrossRef](#)]
27. Li, J.J. Analysis of a series of artificially synthesized Sb₂S₃ (pyroxene)-Sb₂Se₃ (selenoantimonite) solid solutions. In Proceedings of the 9th National X-ray Diffraction Conference and International Centre for Diffraction Data (ICDD) Symposium, Hangzhou, China, 15–17 October 2006. (In Chinese with English Abstract)
28. Liu, J.J.; Liu, J.M.; Xie, H.; Feng, C.X.; Wang, J.P.; Zhang, N.; Li, J.L.; Oi, F. An experimental study on the synthesis of stibnite-antimonelite series. *Miner. Petrol.* **2006**, *26*, 16–23. (In Chinese with English Abstract)

29. Liu, J.J.; Zheng, M.H. First discovery of a selenium-sulfur compound series of antimony. *Chn. Sci. Bull.* **1992**, *37*, 864. (In Chinese with English Abstract)
30. Turekian, K.K.; Wedepohl, K.H. Distribution of the Elements in Some Major Units of the Earth's Crust. *GSA Bull.* **1961**, *72*, 175–192. [[CrossRef](#)]
31. Large, R.R.; Gregory, D.D.; Steadman, J.A.; Tomkins, A.G.; Lounejeva, E.; Danyushevsky, L.V.; Halpin, J.A.; Maslennikov, V.; Sack, P.J.; Mukherjee, I.; et al. Gold in the oceans through time. *Earth Planet. Sci. Lett.* **2015**, *428*, 139–150. [[CrossRef](#)]
32. Liu, J.M.; Liu, J.J. Basin fluid genetic model of sediment-hosted micro disseminated gold deposits in the gold-triangle area between Guizhou, Guangxi and Yunnan. *Mineral. Sin.* **1997**, *17*, 448–456. (In Chinese with English Abstract)
33. Sun, J.G.; Hu, S.X.; Liu, J.M.; Shen, K.; Ling, H.F. Nd, Sr, O isotope study of potassium-rich dark-coloured dyke swarms in the Late Mesozoic gold-mining area, Jiaodong, China. *Acta Geol. Sin.* **2001**, *75*, 553. (In Chinese with English Abstract)
34. Taylor, H. The application of oxygen and hydrogen isotope studies to problems of hydrothermal alteration and ore deposition. *Econ. Geol.* **1974**, *69*, 843–883. [[CrossRef](#)]
35. Sheppard, S. Identification of the origin of oreforming solutions by the use of stable isotopes. *Geol. Soc. Lond. Spec. Publ.* **1977**, *7*, 25–41. [[CrossRef](#)]
36. Sheppard, S.M.F. Stable isotope geochemistry of fluids. *Phys. Chem. Earth* **1981**, *13–14*, 419–445. [[CrossRef](#)]
37. Zhang, H.P. The background values of the precipitation stable isotopes of China. *Site Investig. Sci. Technol.* **1989**, *6*, 6–13.
38. Clayton, R.N.; O'neil, J.R.; Mayeda, T.K. Oxygen isotope exchange between quartz and water. *Geophys. Res.* **1972**, *77*, 3057–3067. [[CrossRef](#)]
39. O'neil, J.R.; Clayton, R.N.; Mayeda, T.K. Oxygen isotope fractionation in divalent metal carbonates. *Chem. Phys.* **1969**, *51*, 5547–5558. [[CrossRef](#)]
40. Luo, X.S. Geological characteristics, mineralisation and direction of searching for antimony ore in E'nan area. *Resour. Environ. Eng.* **2013**, *27* (Suppl. S1), 69–75+80. (In Chinese with English Abstract)
41. Keith, M.; Smith, D.J.; Jenkin, G.R.T.; Holwell, D.A.; Dye, M.D. A review of Te and Se systematics in hydrothermal pyrite from precious metal deposits: Insights into ore-forming processes. *Ore Geol. Rev.* **2018**, *96*, 269–282. [[CrossRef](#)]
42. Schirmer, T.; Koschinsky, A.; Bau, M. The ratio of tellurium and selenium in geological material as a possible paleo-redox proxy. *Chem. Geol.* **2014**, *376*, 44–51. [[CrossRef](#)]
43. Wen, H.; Carignan, J. Selenium isotopes trace the source and redox processes in the black shale-hosted Se-rich deposits in China. *Geochim. Cosmochim. Acta* **2011**, *75*, 1411–1427. [[CrossRef](#)]
44. Guo, Q.; Shields, G.A.; Liu, C.Q.; Strauss, H.; Zhu, M.Y.; Pi, D.H.; Goldberg, T.; Yang, X.L. Trace element chemo stratigraphy of two Ediacaran–Cambrian successions in South China: Implications for organ sedimentary metal enrichment and silicification in the Early Cambrian. *Palaeogeogr. Palaeoclimatol. Palaeoecol.* **2007**, *254*, 194–216. [[CrossRef](#)]
45. Lehmann, B.; Nagler, T.F.; Holland, H.D.; Wille, M.; Mao, J.W.; Pan, J.Y.; Ma, D.S.; Dulski, P. Highly metalliferous carbonaceous shale and Early Cambrian seawater. *Geology* **2007**, *35*, 403–406. [[CrossRef](#)]
46. Xu, L.G.; Lehmann, B.; Mao, J.W. Seawater contribution to polymetallic Ni–Mo–PGE–Au mineralization in Early Cambrian black shales of South China: Evidence from Mo isotope, PGE, trace element, and REE geochemistry. *Ore Geol. Rev.* **2013**, *52*, 66–84. [[CrossRef](#)]
47. Liu, J.M.; Gu, X.X.; Liu, J.J.; Zhen, M.H. Giant metallogenic Sb belt in south China and its constraints. *Acta. Geogr. Sin.* **1998**, *41* (Suppl. S1), 206–215. (In Chinese with English Abstract)
48. Koc, H.; Mamedov, A.M.; Deligoz, E.; Ozisik, H. First principles prediction of the elastic, electronic, and optical properties of Sb₂S₃ and Sb₂Se₃ compounds. *Solid State Sci.* **2012**, *14*, 1211–1220. [[CrossRef](#)]
49. Madelung, O. *Semiconductors: Group IV Elements and III–V Compounds*; Springer Science & Business Media: Berlin/Heidelberg, Germany, 1991.
50. Caracas, R.; Gonze, X. First-principles study of the electronic properties of A₂B₃ minerals, with A = Bi, Sb and B = S, Se. *Phys. Chem. Miner.* **2005**, *32*, 295–300. [[CrossRef](#)]
51. Fu, M.S.; Chen, L.X.; Li, C.Y.; Xu, J.; Chai, D.; Li, Y.Q. Density Functional Theory Study on Crystal Structure and Properties of Arsenic-bearing Pyrite. *Conserv. Util. Min. Resour.* **2022**, *42*, 112–118. (In Chinese with English Abstract)
52. Vavra, G.; Schmid, R.; Gebauer, D. Internal morphology, habit and U-Th-Pb microanalysis of amphibolite-to-granulite facies zircons: Geochronology of the Ivrea Zone (Southern Alps). *Contrib. Mineral. Petrol.* **1999**, *134*, 380–404. [[CrossRef](#)]
53. Zhang, Z.M.; Wang, J.L.; Shen, K.; Shi, C. Paleozoic circum-Gondwana orogens: Petrology and geochronology of the Namche Barwa Complex in the eastern Himalayan syntaxis, Tibet. *Acta Petrol. Sin.* **2008**, *24*, 1627–1637. (In Chinese with English Abstract)
54. Miller, C.F.; Hatcher, R.D., Jr.; Mark, H.T.; Coath, C.D.; Gorisch, E.B. Cryptic crustal events elucidated through zone imaging and ion microprobe studies of zircon, southern Appalachian Blue Ridge, North Carolina–Georgia. *Geology* **1998**, *26*, 419–422. [[CrossRef](#)]
55. Schaltegger, U.; Fanning, C.M.; Gunther, D.; Maurin, J.C.; Schulmann, K.; Gebauer, D. Growth, annealing and recrystallization of zircon and preservation of monazite in high-grade meta morphism: Conventional and in-situ U-Pb isotope, cathodoluminescence and microchemical evidence. *Contrib. Mineral. Petrol.* **1999**, *134*, 186–201. [[CrossRef](#)]
56. Liu, X.; Tang, Y.J. The characteristics and implication of the zonation in clinopyroxene phenocrysts from the Yaojiazhuang ultramafic-syenitic complex, northwestern Hebei Province. *Acta Petro. Sin.* **2018**, *34*, 3315–3326. (In Chinese with English Abstract)

57. Nisbet, E.G.; Pearce, J.A. Clinopyroxene composition in mafic lavas from different tectonic settings. *Contrib. Mineral. Petrol.* **1977**, *63*, 149–160. [[CrossRef](#)]
58. Dobosi, G. Clinopyroxene zoning patterns in the young alkali basalts of Hungary and their petrogenetic significance. *Contrib. Mineral. Petrol.* **1989**, *101*, 112–121. [[CrossRef](#)]
59. Zhang, W.Y.; Wang, C.Z.; Sun, Y.C.; Qiu, Z.Z.; Cu, Y.B. Characteristics of zonal pyrite in Zijinshan Cu-Au Deposit. *Nonferrous Met. (Min. Sec.)* **2014**, *66*, 36–42. (In Chinese with English Abstract)
60. Zhang, D.Q.; Li, D.X.; Zhao, Y.M.; Chen, J.H.; Li, Z.L.; Zhang, K.Y. The Zijinshan deposit: The first example of quartz-alunite type epithermal deposits in the continent of China. *Geol. Rev.* **1991**, *37*, 481–491. (In Chinese with English Abstract)
61. Liu, H.P.; Zhang, Y.L.; Hu, W.Q. On the origin of the stibnite deposit of Shikuangshan mine, Hunan. *Hunan Geol.* **1985**, *4*, 28–39+83. (In Chinese with English Abstract)
62. Simon, G.; Essene, E.J. Phase relations among selenides, sulfides, tellurides, and oxides; I, Thermodynamic properties and calculated equilibria. *Eco. Geol.* **1996**, *91*, 1183–1208. [[CrossRef](#)]
63. Simon, G.; Kesler, S.E.; Essene, E.J. Phase relations among selenides, tellurides, and oxides; II, Applications to selenide-bearing ore deposits. *Eco. Geol.* **1997**, *92*, 468–484. [[CrossRef](#)]

Disclaimer/Publisher’s Note: The statements, opinions and data contained in all publications are solely those of the individual author(s) and contributor(s) and not of MDPI and/or the editor(s). MDPI and/or the editor(s) disclaim responsibility for any injury to people or property resulting from any ideas, methods, instructions or products referred to in the content.